Arabian Journal of Chemistry (2018) xxx, xxx–xxx

King Saud University

Arabian Journal of Chemistry

www.ksu.edu.sa
www.sciencedirect.com

ORIGINAL ARTICLE

Tuning the morphological structure, light absorption, and photocatalytic activity of Bi_2WO_6 and Bi_2WO_6-BiOCl through cerium doping

Mirabbos Hojamberdiev [a,b,*], Zukhra C. Kadirova [c], Ehsan Zahedi [d], Diego Onna [e], María Claudia Marchi [e], Gangqiang Zhu [f], Nobuhiro Matsushita [a], Masashi Hasegawa [b], Sara Aldabe Bilmes [e], Kiyoshi Okada [a]

[a] *Materials and Structures Laboratory, Tokyo Institute of Technology, 4259 Nagatsuta, Midori, Yokohama 226-8503, Kanagawa, Japan*
[b] *Department of Materials Physics, Nagoya University, Furo-cho, Chikusa-ku, Nagoya 464-8603, Japan*
[c] *Uzbekistan-Japan Youth Innovation Center, Tashkent 100095, Uzbekistan*
[d] *Department of Physical Chemistry, Shahrood Branch, Islamic Azad University, Shahrood, Iran*
[e] *Instituto de Química Física de los Materiales, Medio Ambiente y Energía (INQUIMAE), Facultad de Ciencias Exactas y Naturales, Universidad de Buenos Aires, Pabellón II, Ciudad Universitaria, C1428EHA Buenos Aires, Argentina*
[f] *School of Physics and Information Technology, Shaanxi Normal University, Xi'an 710062, China*

Received 28 January 2018; accepted 21 July 2018

KEYWORDS

Bi_2WO_6;
BiOCl;
Salicylic acid;
Water pollutant;
Photocatalyst;
Cerium doping

Abstract Pharmaceuticals and personal care products are recognized as new classes of water pollutants that receive considerable attention because of their negative environmental impact on aquatic life and humans. Because microbiological and/or conventional secondary physicochemical treatments cannot completely remove those water pollutants, effective advanced oxidation processes using semiconductor-based photocatalysts are needed to ensure their total elimination in water. Here, we report on the tuning of the morphological structure, light absorption, and photocatalytic activity of Bi_2WO_6 and Bi_2WO_6-BiOCl through cerium doping. Non-doped and Ce-doped Bi_2WO_6 and Bi_2WO_6-BiOCl powders are synthesized by a hydrothermal method, and their adsorption ability and photocatalytic activity are evaluated for the removal of salicylic acid in the dark and under visible light irradiation, respectively. The adsorption affinities and preferential sites of salicylic acid molecules on non-doped and Ce-doped Bi_2WO_6, BiOCl, and Bi_2WO_6-BiOCl are computationally predicted using molecular dynamics simulations. When ethylene glycol is replaced by

* Corresponding author at: Department of Materials Physics, Nagoya University, Furo-cho, Chikusa-ku, Nagoya 464-8603, Japan.
E-mail address: hmirabbos@mp.pse.nagoya-u.ac.jp (M. Hojamberdiev).
Peer review under responsibility of King Saud University.

Production and hosting by Elsevier

https://doi.org/10.1016/j.arabjc.2018.07.014

Please cite this article in press as: Hojamberdiev, M. et al., Tuning the morphological structure, light absorption, and photocatalytic activity of Bi_2WO_6 and Bi_2WO_6-BiOCl through cerium doping. Arabian Journal of Chemistry (2018), https://doi.org/10.1016/j.arabjc.2018.07.014

dilute HCl as a solvent in a hydrothermal system, BiOCl is also formed along with Bi_2WO_6, confirming the successful formation of a Bi_2WO_6-BiOCl composite. The flower-like hierarchical structures of Bi_2WO_6 and Bi_2WO_6-BiOCl can absorb more photon energy due to multiple scattering, charge carriers can easily transfer to the surface/interface, and mesopores can improve the transfer rate of organic molecules, contributing to the overall enhancement in photocatalytic activity. The Bi_2WO_6-BiOCl samples show higher photocatalytic activity than that of the Bi_2WO_6 samples for the degradation of salicylic acid due to the formed *p–n* heterojunction. The optimum concentration of Ce doping is found to be 1 mol% in the Bi_2WO_6 and Bi_2WO_6-BiOCl, promoting the effective separation and transfer of photogenerated charge carriers, resulting in high photocatalytic performance, and the sample exhibited good stability.

1. Introduction

As one of the simplest members of the Aurivillius oxide family, Bi_2WO_6 is composed of perovskite-like $[WO_4]^{2-}$ layers sandwiched between bismuth oxide $[Bi_2O_2]^{2+}$ layers, favoring the efficient separation of photogenerated electron–hole pairs and improving the photocatalytic activity because of the formed internal electric fields between the slabs (Zhang et al., 2014; Zhu et al., 2014). Recent studies have demonstrated that the photocatalytic performance of Bi_2WO_6 can be enhanced by compositing with other semiconductors, such as $BiVO_4$ (Ju et al., 2014), WO_3 (Peng et al., 2015), Fe_3O_4 (Xu et al., 2012), $ZnWO_4$ (Hojamberdiev et al., 2013), and $CeVO_4$ (Hojamberdiev et al., 2017a), BiOI (Hojamberdiev et al., 2017b), and reduced graphene oxide (Hojamberdiev et al., 2018).

Particularly, to improve its photocatalytic performance, Bi_2WO_6 was composited with BiO*X* (*X* = Cl, Br, and I), which are important V–VI–VII ternary semiconductor compounds that have a tetragonal matlockite structure, a layered structure characterized by $[Bi_2O_2]$ slabs interleaved by double slabs of halogen atoms (Ye et al., 2014). For instance, a BiOCl–Bi_2WO_6 heterojunction with a chemically bonded interface was synthesized via a facile one-step solvothermal method and yielded a high photodegradation rate of rhodamine B under visible light irradiation due to the favorable band offsets across the Bi_I–O–Bi_{II} bonded interface, leading to efficient interfacial charge carrier transfer (Yang et al., 2013). In comparison with the BiOBr–Bi_2WO_6 nanosheet composite, the BiOBr–Bi_2WO_6 mesoporous nanosheet composite prepared by using a facile hydrothermal synthetic route with a controlled fraction of Ti$(O^iPr)_4$ exhibited a much improved photocatalytic activity under visible light irradiation because of (i) the large specific surface area with hierarchical pore sizes and a highly exposed BiOBr (0 0 1) facet, (ii) the evidently enhanced charge separation efficiency, and (iii) high light harvesting efficiency (Li et al., 2013). The stable 30%Bi_2WO_6/BiOI heterojunction photocatalyst synthesized using a facile hydrothermal method based on the efficient chemical etching principle showed high visible-light-induced photocatalytic and antibacterial activities for the degradation of methylene blue and the killing of *P. aeruginosa*, *E. coli*, and *S. aureus* owing to the efficient separation of photogenerated electron–hole pairs on the formed *p–n* heterojunction (Xiang et al., 2016).

In recent years, doping with lanthanide ions, such as La^{3+} (Wang et al., 2016a), Sm^{3+}/Sm^{2+} (Wang et al., 2016b), Eu^{3+} (Tian et al., 2012), Gd^{3+} (Tian et al., 2014), Ho^{3+} (Li et al., 2017a), Er^{3+} (Wang et al., 2015), and Yb^{3+} (Li et al., 2017a), has shown to be an efficient approach to improve the photocatalytic activity of Bi_2WO_6 because of their unique optical properties and 4f electron configuration.

As a common emerging water pollutant, salicylic acid (2-hydroxybenzoic acid) is widely used in the production of cosmetics, food, and pharmaceutical (a main precursor of aspirin) and dermatological products (Stamatis and Konstantinou, 2013). Due to its widespread use, salicylic acid has been consistently detected up to relatively high concentrations of 50 $\mu g \cdot L^{-1}$ in surface water (Kosma et al., 2014) and 89.1 $\mu g \cdot L^{-1}$ in the effluents of municipal wastewater treatment plants (Evgenidou et al., 2015). As an example, aspirin degrades in an aqueous medium into several toxic intermediates causing environmental pollution, which ultimately affects human health (Mukherjee et al., 2016; SCCNFP/0522/01, final, 2002). However, microbiological and/or conventional secondary physicochemical treatments (Sirés and Brillas, 2012) cannot completely remove salicylic acid. Therefore, effective advanced oxidation processes are needed to ensure the total elimination of salicylic acid in water.

Very recently, the immobilized photocatalytic structures of self-organized and well-aligned TiO_2 nanotubular films fabricated by galvanostatic anodization demonstrated a slightly higher efficiency for the degradation of salicylic acid compared with that of TiO_2-P25 at alkaline to acidic pH values due to the easy removal of the formed intermediates from the highly porous surface (Arfanis et al., 2017). Ma et al. (2017) synthesized magnetically separable F-N co-doped TiO_2 using a facile sol-gel method grafted on magnetically activated carbon decorated with carbonized chitosan and found that the degradation of salicylic acid under visible light irradiation was strongly dependent on the molar ratio of F:Ti. A 3.0 L solar flow plant with a Pt/air-diffusion (anode/cathode) cell, a solar photoreactor and a photocatalytic photoreactor filled with TiO_2-coated glass spheres was utilized to couple solar photoelectro-Fenton (SPEF) and solar heterogeneous photocatalysts (SPC) for the efficient mineralization of salicylic acid (Garza-Campos et al., 2016).

The present study aims at tuning the morphological structure, light absorption, and photocatalytic activity of Bi_2WO_6 and Bi_2WO_6-BiOCl through cerium doping. The adsorption and photocatalytic activities of pure and Ce-doped Bi_2WO_6 and Bi_2WO_6-BiOCl powders were evaluated for the removal of salicylic acid, as an emerging water pollutant in the dark and under visible light irradiation. It was found that the cerium doping can effectively improve the photocatalytic activity, and the use of Ce-doped Bi_2WO_6 and Bi_2WO_6-BiOCl powders

Please cite this article in press as: Hojamberdiev, M. et al., Tuning the morphological structure, light absorption, and photocatalytic activity of Bi_2WO_6 and Bi_2WO_6-BiOCl through cerium doping. Arabian Journal of Chemistry (2018), https://doi.org/10.1016/j.arabjc.2018.07.014

can be extended to the degradation of other organic pollutants in water.

2. Experimental

2.1. Synthesis

Pure and cerium-doped Bi_2WO_6 and Bi_2WO_6-BiOCl powders were synthesized by a hydrothermal method. The experimental procedures were as follows. For pure and Ce-doped Bi_2WO_6, 2–x mmol of $Bi(NO_3)_3{\cdot}5H_2O$ ($\geq$ 98.0%, Sigma-Aldrich), x mol of $CeCl_3{\cdot}7H_2O$ (x = 0, 0.5, 1, 2, 4, 6, 8 and 10 mol%) (99.9%, Sigma-Aldrich), and 2 mmol of $Na_2WO_4{\cdot}2H_2O$ (99%, Alfa Aesar) were dissolved in 10 mL of ethylene glycol (99.8%, Sigma-Aldrich) and 15 and 15 mL of deionized water. For pure and Ce-doped Bi_2WO_6-BiOCl, 2–x mmol of $Bi(NO_3)_3{\cdot}5H_2O$, x mol of $CeCl_3{\cdot}7H_2O$ (x = 0, 0.5, 1, 2, 4, 6, 8 and 10 mol%), and 2 mmol of $Na_2WO_4{\cdot}2H_2O$ were dissolved in 2 mL of dilute HCl and 18 and 20 mL of deionized water. After being well homogenized under vigorous magnetic stirring for 30 min, the pH of the suspension was adjusted to 9 by the dropwise addition of 28% aqueous ammonia solution (Merck), and the suspension was transferred into a Teflon-lined stainless steel autoclave with a filling capacity of 75% and maintained at 180 °C for 12 h. The resultant precipitate was collected, washed with deionized water several times and dried at 100 °C for 12 h.

2.2. Characterization

X-ray diffraction (XRD) patterns were acquired with a Siemens D5000 diffractometer using Cu Kα radiation (λ = 0.15418 nm) in the 2 θ scan range from 10 to 70° and compared with entries from the ICDD-PDF-2 powder pattern database. The particle morphologies and sizes of the synthesized samples were examined using a ZEISS Supra 40 VP scanning electron microscope. The ultraviolet–visible (UV–vis) diffuse reflectance spectra were recorded on a Lambda 20 UV–vis spectrometer (PerkinElmer, Inc.) equipped with an integrating sphere, and $BaSO_4$ was used as a reference. The optical absorption spectra were converted from the UV–vis diffuse reflectance spectra using the Kubelka–Munk function, $F(R) = (1 - R)^2/2R = k/s$, where R is the absolute reflectance of the sampled layer, k is the molar absorption coefficient, and s is the scattering coefficient. A zeta potential analyzer (Zeta-PALS, Brookhaven Instruments Corporation) was used to characterize the electrokinetic potential of pure and Ce-doped Bi_2WO_6 and Bi_2WO_6-BiOCl particles in colloidal dispersions. For the zeta-potential measurements at a neutral pH adjusted by a NaOH aqueous solution, the suspension was prepared by dispersing the as-synthesized powders in deionized water under continuous magnetic stirring. The specific surface areas (S_{BET}) of the samples were determined by the Brunauer–Emmett–Teller (BET) method from the linear portion of the nitrogen gas adsorption isotherms measured at –196 °C using an Autosorb-1A (Quantachrome Instruments). The surface chemical composition and elemental states were analyzed by X-ray photoelectron spectroscopy (JPS-9010MC, JEOL) using nonmonochromated Mg Kα radiation (1253.6 eV) with a 10 mA emission current and a 10 kV acceleration voltage. The XPS profiles were fitted using a Gaussian–Lorentzian function, and the peak positions were normalized by positioning the C 1s peak at 284.5 eV. The chemical compositions of the samples were analyzed by X-ray fluorescence (RIX2000, Rigaku).

2.3. Photocatalytic activity test

To study the effect of cerium doping, salicylic acid was selected as the probe molecule to evaluate the adsorption and photocatalytic activities of Ce-doped Bi_2WO_6 and Bi_2WO_6-BiOCl photocatalysts under visible light irradiation. The photodegradation of salicylic acid by the hydrothermally synthesized samples was performed in a 60 mL glass-tube reactor under simulated solar light using a 300 W Xe lamp (AM1.5G filter; 18.5 $mW{\cdot}cm^{-2}$). The photodegradation reaction temperature was maintained at 25 °C by water flowing through the cooling jacket of the reactor. The initial concentration of salicylic acid in aqueous solution was 25 $mg{\cdot}L^{-1}$, and the photocatalyst sample content was 1.0 $g{\cdot}L^{-1}$. First, the photocatalyst sample was dispersed in a glass vial containing a 50 mL of salicylic acid in an aqueous solution, and the suspension was stirred in the dark for 2 h to ensure adsorption–desorption equilibrium prior to simulation with solar light irradiation. During the photodegradation reaction, 2 mL of the suspension was taken out at a predetermined time interval for subsequent analysis of the salicylic acid concentration. The concentration of salicylic acid was analyzed by a U-3010 UV–vis spectrophotometer (Hitachi) by measuring the change in the intensity of the absorption peaks of salicylic acid at 296 nm. The total organic carbon (TOC) content of the solution was analyzed using a total organic carbon analyzer (5050A, Shimadzu).

3. Results and discussion

The crystal structures of the as-synthesized samples were characterized by powder X-ray diffraction. The XRD patterns of the samples doped with different contents of cerium ranging from 0 mol% to 10 mol% are shown in Fig. 1 with the International Center for Diffraction Data Powder Diffraction File (ICDD PDF) data. As shown in Fig. 1a, the diffraction lines in the XRD pattern of the sample hydrothermally synthesized using ethylene glycol as a solvent correspond to orthorhombic Bi_2WO_6 with a space group of $Pca2_1$ (ICDD PDF# 39–0256), confirming the phase purity of Bi_2WO_6. The diffraction lines in the XRD pattern of the sample hydrothermally synthesized using dilute HCl as a solvent are in good agreement with the orthorhombic phase of Bi_2WO_6 (ICDD PDF# 39–0256) and the tetragonal phase of BiOCl with a space group of $P4/nmm$ (ICDD PDF# 06–0249), indicating the co-existence of the Bi_2WO_6 and BiOCl phases in the sample (Fig. 1b). Along with Bi_2WO_6, the BiOCl phase was also formed because of a rapid reaction of Bi^{3+} and the available Cl^- ions dissociated from HCl in the synthesis solution:

$$Bi^{3+}(aq) + Cl^-(aq) + H_2O(l) \rightarrow BiOCl(s) + 2H^+(aq).$$

Since the effective ionic radius of Ce^{3+} (r_{ion} = 1.01 Å for CN = 6) is very similar to that of Bi^{3+} (r_{ion} = 1.03 Å for CN = 6), there is no significant shift in the 2θ angle of the diffraction patterns, demonstrating that the Bi^{3+} ions were substitutionally replaced by the Ce^{3+} ions in the alternatively stacked $[Bi_2O_2]^{2+}$ layers of the Bi_2WO_6 and BiOCl crystal

Please cite this article in press as: Hojamberdiev, M. et al., Tuning the morphological structure, light absorption, and photocatalytic activity of Bi_2WO_6 and Bi_2WO_6-BiOCl through cerium doping. Arabian Journal of Chemistry (2018), https://doi.org/10.1016/j.arabjc.2018.07.014

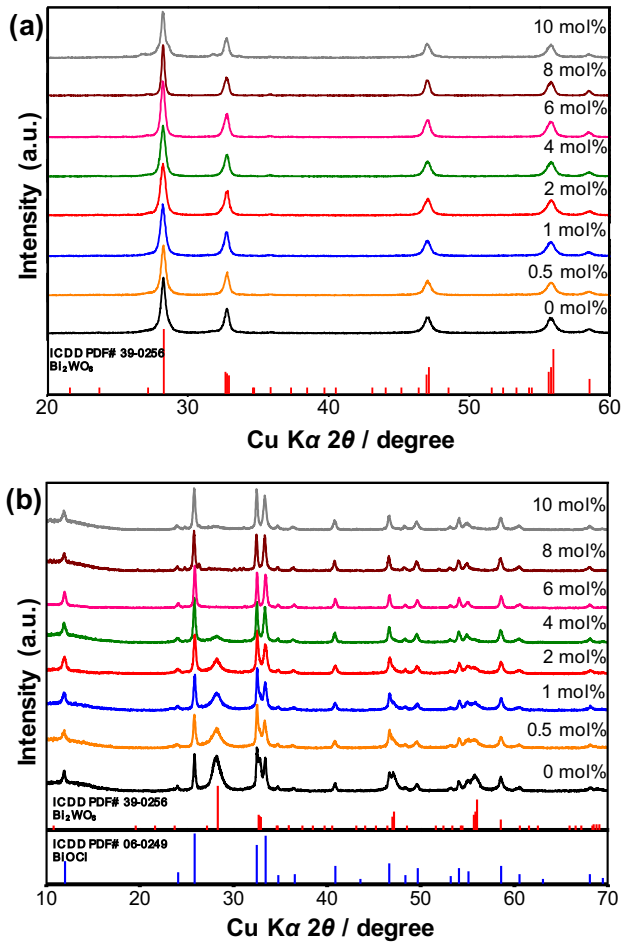

Fig. 1 XRD patterns of (a) Bi_2WO_6 and (b) Bi_2WO_6-BiOCl powders doped with different contents of cerium ranging from 0 mol% to 10 mol%.

structures. Notably, an increase in the Ce content up to 10 mol % neither segregated the Ce-rich phases nor changed the preferential orientations, implying that all doped cerium ions were fully accommodated into the Bi_2WO_6 and BiOCl lattices. However, an increase in the Ce content up to 4 mol% gradually decreased the content of the Bi_2WO_6 phase in the sample, while the BiOCl phase became more predominant due to the increase in the concentration of the Cl^- ions in the synthesis solution highly saturated with cerium trichloride. From 6 mol% to 10 mol% Ce, the Bi_2WO_6 phase completely vanished, leaving behind BiOCl as a single phase. The diffraction lines resulting from the {1 1 1} plane of the Bi_2WO_6 and BiOCl crystals are obviously stronger compared to other diffraction lines, confirming the dominance of the {1 1 1} plane in the synthesized crystals. It is thought that the Ce^{2+} and Ce^{4+} ions were unlikely formed under the current synthesis conditions applied in this study. The XRD results suggest that the selection of a solvent type (ethylene glycol or dilute HCl) and the content of cerium dopants are important for the synthesis of the phase-pure Ce-doped Bi_2WO_6 and Bi_2WO_6-BiOCl powders.

The morphology and microstructure of the as-synthesized samples were examined by scanning electron microscopy, and the results are represented in Figs. 2 and 3. Fig. 2 shows the typical SEM images of the non-doped and Ce-doped Bi_2WO_6 powders. As depicted in Fig. 2a, non-doped Bi_2WO_6 powders exhibit hierarchical, not well-defined, structures with an average diameter of less than 3 μm. These hierarchical structures were assembled by a random aggregation of numerous nanosheets with a thickness of approximately 25 nm. Interestingly, with an increasing content of cerium dopant up to 6 mol%, these hierarchical structures gained their clear flower-like morphology constructed by parallelly and perpendicularly stacked nanosheets (Fig. 2b–f). A further increase in the content of cerium dopant to 8 mol% led to the formation of acicular crystals on the surface of these flower-like hierarchical structures (Fig. 2g), which were ultimately converted into the aggregated acicular nanocrystals at 10 mol% Ce (Fig. 2h). Apparently, the thickness of the Bi_2WO_6 nanosheets was gradually reduced with increasing content of cerium dopant. Here, ethylene glycol was used as a solvent as well as a complexing agent forming a chain structure on the surface of the crystallites via either covalent or hydrogen bonding. During the hydrothermal reaction, Bi_2WO_6 nuclei were formed first and served as seeds for the growth of Bi_2WO_6 nanosheets in the supersaturated solution. Due to its high intrinsic anisotropic nature, Bi_2WO_6 grew into two-dimensional nanosheets. Further, the nanosheets with a high anisotropic surface energy were self-assembled readily into flower-like hierarchical structures through an ethylene glycol-induced Ostwald ripening (Wang et al., 2014; Cui et al., 2016). For the non-doped Bi_2WO_6-BiOCl composite, irregularly shaped nanosheets with an average size of 350 nm, which did not form flower-like hierarchical structures, are shown in Fig. 3a. When the cerium was doped, the randomly distributed nanosheets of the non-doped composite were gradually transformed into mostly parallel intersected nanoplates with scalloped edges due to acid etching (Xu et al., 2018), resulting in the flower-like hierarchical structures with the size of approximately 3 μm (Fig. 3b–f), and the nanoplates became completely dominant in the range of 6–10 mol% Ce. Strikingly, at 8 and 10 mol% Ce, the distance between the stacked nanoplates was significantly shortened, and a greater number of enlarged nanoplates were parallelly stacked (compactly packed) to form spherical structures (Fig. 3g and h). On one hand, the morphological transformation can be interpreted by the gradual dominance of the BiOCl phase over the Bi_2WO_6 phase in the composite. On the other hand, as most cerium ions were substitutionally introduced into BiOCl and Bi_2WO_6 without a noticeable lattice distortion, the selective adsorption of excessive Cl^- ions on specific crystal facets possibly governed the crystal growth, leading to the morphological variation with increasing concentration of cerium trichloride in the synthesis solution (An et al., 2008). These flower-like hierarchical structures can absorb more photon energy due to multiple scattering, the photogenerated charge carriers can easily transfer to the surface/interface because of the nanoscale thickness of the nanosheets, and the mesopores of the synthesized samples can improve the transfer rate of the organic molecules, which contribute to the enhancement in the photocatalytic activity of the synthesized samples.

The surface chemical compositions and chemical states of the as-synthesized samples (non-doped and 2 mol% Ce-doped Bi_2WO_6 and Bi_2WO_6-BiOCl) were investigated by X-ray photoelectron spectroscopy (XPS), and the Bi 4f, W 4f, O 1s, Cl 2p, and Ce 3d XPS core-level spectra of the samples are shown in Fig. 4. The XPS peaks centered at 164.6 and 159.3 eV can be assigned to the binding energies

Please cite this article in press as: Hojamberdiev, M. et al., Tuning the morphological structure, light absorption, and photocatalytic activity of Bi_2WO_6 and Bi_2WO_6-BiOCl through cerium doping. Arabian Journal of Chemistry (2018), https://doi.org/10.1016/j.arabjc.2018.07.014

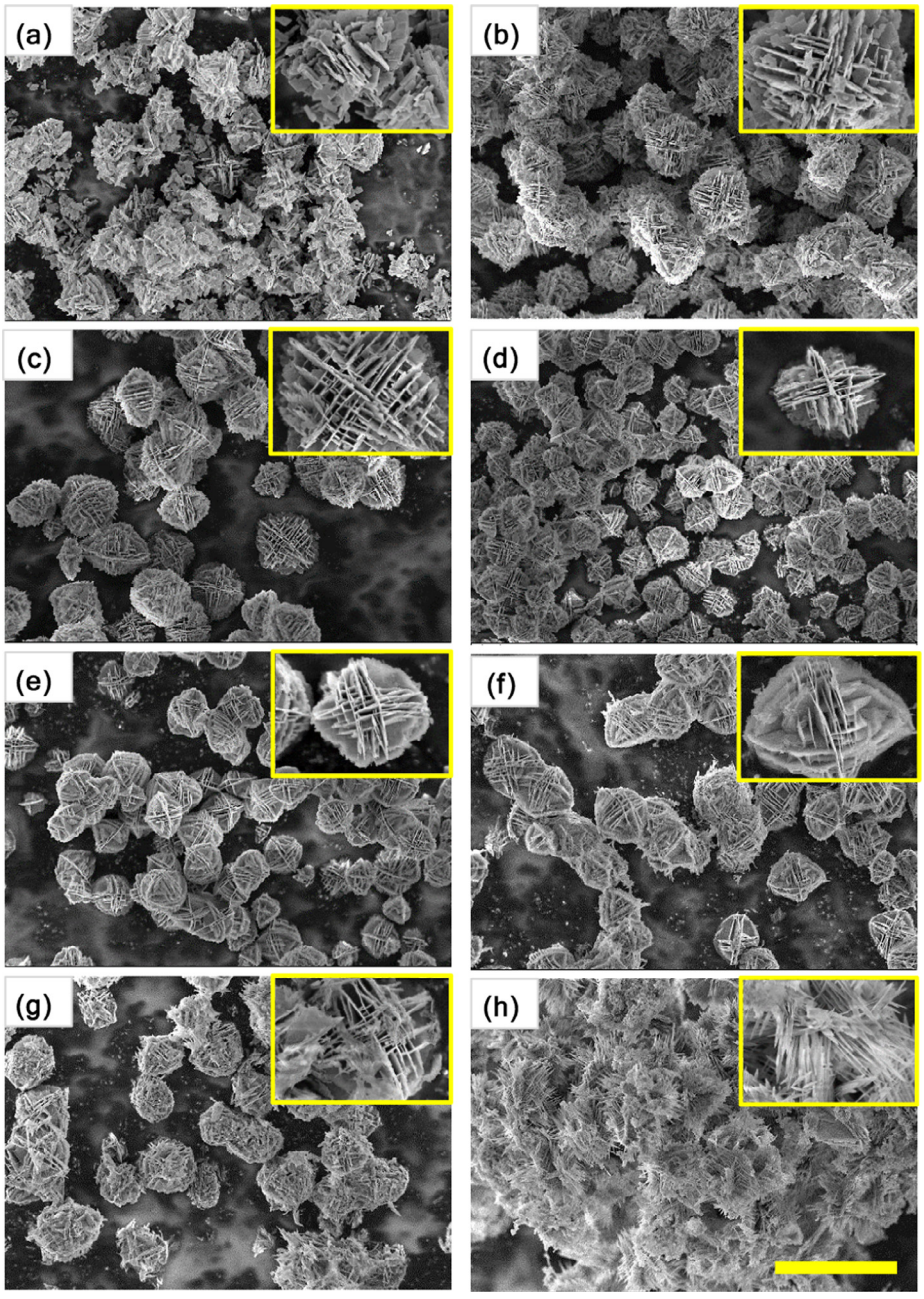

Fig. 2 SEM images of Bi_2WO_6 powders doped with different contents of cerium: (a) 0 mol%, (b) 0.5 mol%, (c) 1 mol%, (d) 2 mol%, (e) 4 mol%, (f) 6 mol%, (g) 8 mol%, and (h) 10 mol%. The scale bar is 5 μm.

of Bi $4f_{5/2}$ and Bi $4f_{7/2}$, respectively, indicating that bismuth has an oxidation state of +3. The XPS peaks centered at 37.1 and 34.9 eV can be ascribed to the binding energies of W $4f_{5/2}$ and W $4f_{7/2}$, respectively, confirming that the tungsten has an oxidation state of +6. The O 1s binding energy of 530.8 eV can be attributed to the lattice oxygen in Bi_2WO_6 and BiOCl, and no other pronounced peaks characteristic of the chemisorbed or dissociated oxygen species are noted. In the XPS spectra of Cl 2p, the binding energies of Cl $2p_{1/2}$ and Cl $2p_{3/2}$ are observed at 199.4 and 197.8 eV, respectively, which is the characteristic of Cl^- in BiOCl. The Ce 3d XPS spectra can be deconvoluted into two pairs of spin-orbital bands: Ce^{3+} $3d_{3/2}$ and Ce^{3+} $3d_{5/2}$ at 906.7 and 888.6 eV, respectively and Ce^{4+} $3d_{3/2}$ and Ce^{4+} $3d_{5/2}$ at 903.1 and 885.3 eV, respectively (Francisco et al., 2001). To determine an exact content of cerium doped in the prepared photocatalysts, the X-ray fluorescence spectroscopy (XRF) analysis was performed. According to the XRF results, about 0.99, 2.01, 3.92, 5.93, 7.98, and 9.90% Ce were detected in the Bi_2WO_6 and Bi_2WO_6-BiOCl samples doped with 1, 2, 4, 6, 8, and 10 mol.% Ce, respectively. The obtained values are very close to the theoretical content of Ce, confirming the successful doping of cerium in the Bi_2WO_6 and Bi_2WO_6-BiOCl samples.

The UV–vis diffuse reflectance spectra were measured to evaluate the light absorption properties of the as-synthesized samples. As shown in Fig. 5, pure Bi_2WO_6 (Fig. 5a, black line)

Please cite this article in press as: Hojamberdiev, M. et al., Tuning the morphological structure, light absorption, and photocatalytic activity of Bi_2WO_6 and Bi_2WO_6-BiOCl through cerium doping. Arabian Journal of Chemistry (2018), https://doi.org/10.1016/j.arabjc.2018.07.014

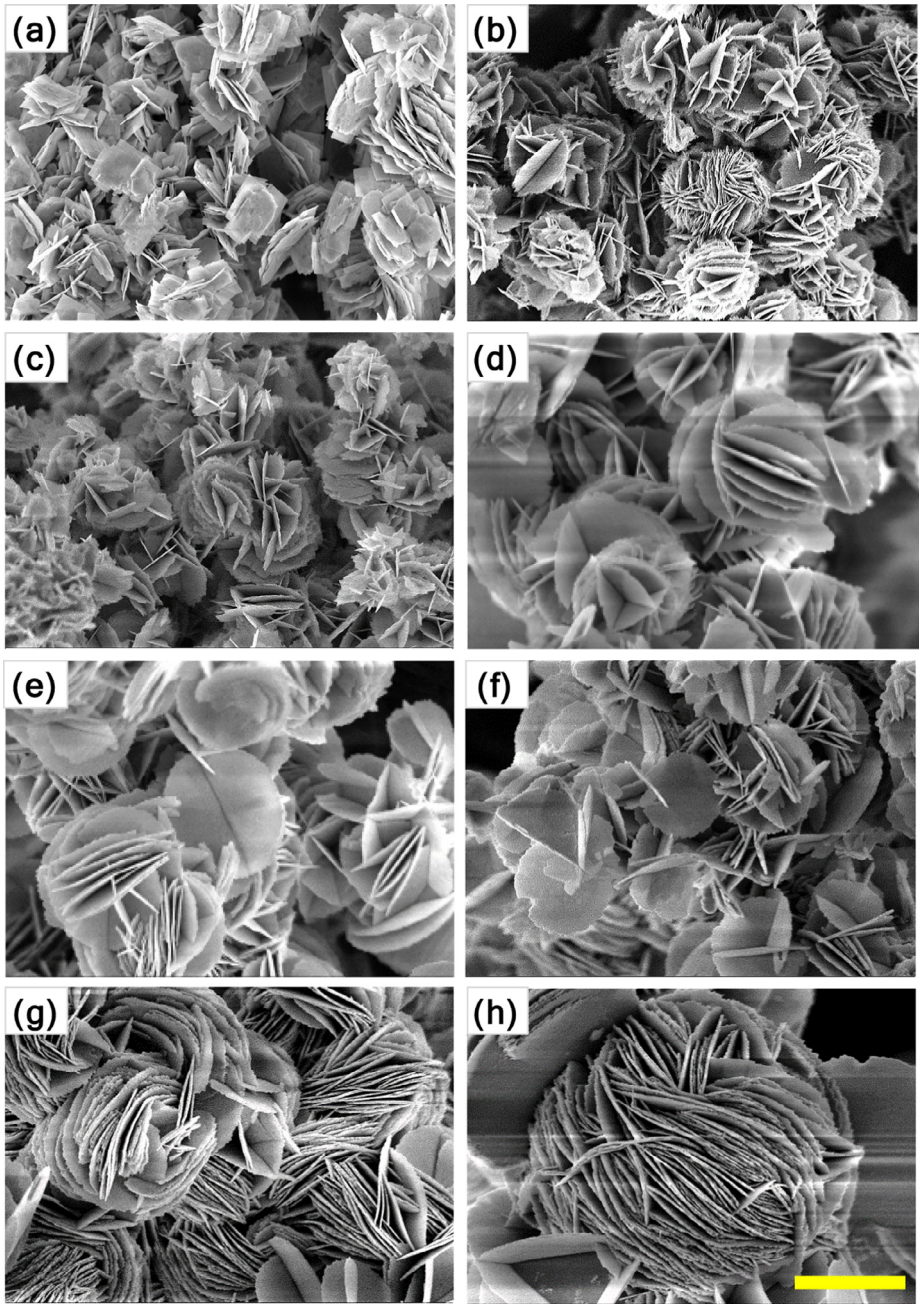

Fig. 3 SEM images of Bi_2WO_6-BiOCl powders doped with different contents of cerium: (a) 0 mol%, (b) 0.5 mol%, (c) 1 mol%, (d) 2 mol%, (e) 4 mol%, (f) 6 mol%, (g) 8 mol%, and (h) 10 mol%. The scale bar is 1 μm.

displays a typical absorption edge at approximately 460 nm, whereas pure Bi_2WO_6-BiOCl (Fig. 5b, black line) shows a slightly lower absorption edge at approximately 450 nm in the visible range owing to the incorporation of the BiOCl. For Ce-doped Bi_2WO_6, the absorption edge is significantly extended up to >700 nm and the intensity of the background absorption is markedly increased with the increasing content of cerium dopant in Bi_2WO_6 from 0 to 10 mol%, which is possibly due to the formation of defects. Interestingly, the Ce-doped Bi_2WO_6-BiOCl samples indicated a smaller redshift (up to 600 nm with 10 mol% Ce) of the absorption band compared to that of the Ce-doped Bi_2WO_6 samples. This finding is because most cerium ions were incorporated into the BiOCl lattice rather than in the Bi_2WO_6 lattice. The redshift in the absorption spectra can be ascribed to the charge transfer between the Bi_2WO_6 and BiOCl valence or conduction bands and the cerium ion 4f level. The corresponding band gap energies calculated from the Tauc plot of $(\alpha h\nu)^{1/2}$ versus photon energy ($h\nu$) for the Bi_2WO_6 and Bi_2WO_6-BiOCl samples with increasing cerium dopant content follow the order: 2.71 and 2.77 eV for 0 mol% Ce > 2.44 and 2.50 eV for 0.5 mol% Ce > 2.23 and 2.26 eV for 1 mol% Ce > 2.00 and 2.22 eV for 2 mol% Ce > 1.93 and 2.21 eV for 4 mol% Ce > 1.80 and 2.17 eV for 6 mol% Ce > 1.67 and 2.13 eV for 8 mol%

Please cite this article in press as: Hojamberdiev, M. et al., Tuning the morphological structure, light absorption, and photocatalytic activity of Bi_2WO_6 and Bi_2WO_6-BiOCl through cerium doping. Arabian Journal of Chemistry (2018), https://doi.org/10.1016/j.arabjc.2018.07.014

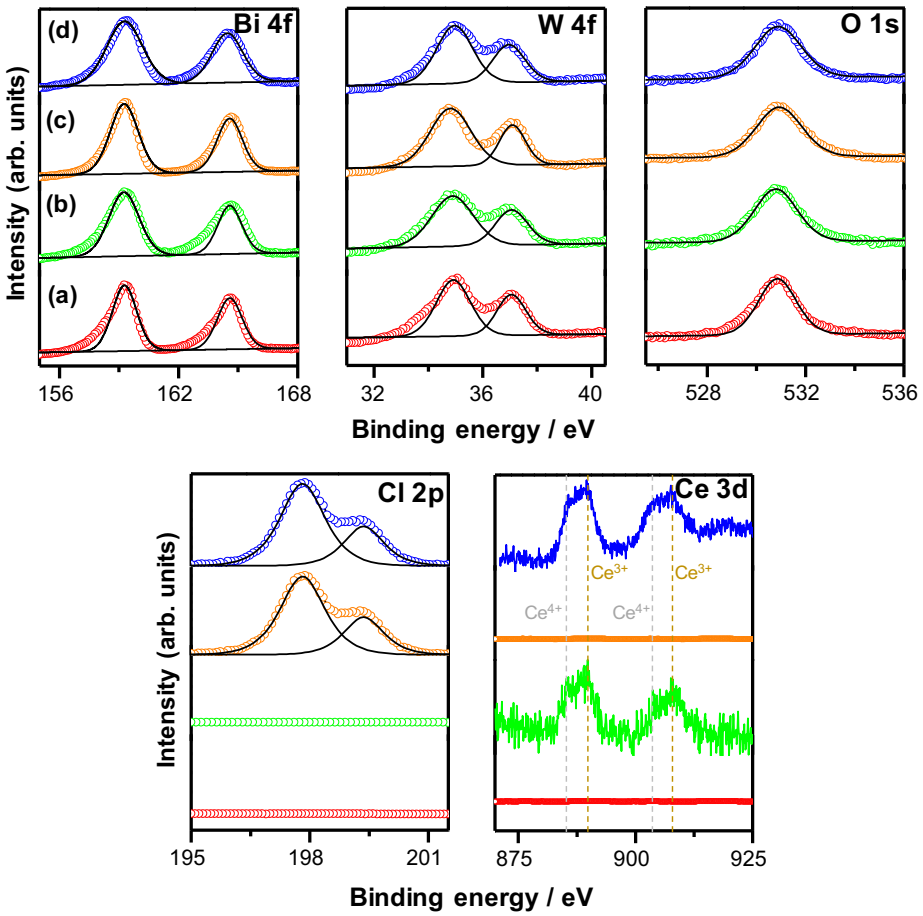

Fig. 4 XPS core-level spectra of Bi 4f, W 4f, O 1s, Cl 2p, and Ce 3d of non-doped (a,c) and 2 mol% Ce-doped (b, d) Bi_2WO_6 and Bi_2WO_6-BiOCl powders.

Ce > 1.37 and 2.11 eV for 10 mol% Ce. This sequence implies that the addition of cerium plays an important role in changing the optical properties, utilizing the visible light of solar energy, and enhancing the photocatalytic activity of Bi_2WO_6 and Bi_2WO_6-BiOCl.

Fig. 6 shows the zeta-potential values of non-doped and Ce-doped Bi_2WO_6 and Bi_2WO_6-BiOCl powders as a function of the cerium dopant content. As shown, both samples indicate no point of zero charge and exhibit negative zeta-potential values at the neutral pH of deionized water, indicating that the as-synthesized samples have negatively charged surfaces. The surface charge of the as-synthesized samples mainly result from the edge surfaces and structural charge sites. The edge surface charge comes from proton adsorption by the hydroxyl groups, whereas the structural charge sites have permanent negative charges. Compared with Bi_2WO_6, the Bi_2WO_6-BiOCl powders possess a greater negative charge due to the presence of Cl^- ions on the surface of BiOCl, creating negatively charged monolayers, which are eventually replaced partly by OH^- because of a surface hydration. Adjacent hydroxyl groups interact with the particle surface during the formation of a hydrated layer, which may result in hydrogen bonding between neighboring hydroxyl groups. In both cases, cerium doping may possibly reduce the negative charge values that provide a less favorable environment for the adsorption of negatively charged hydroxyl groups on the surfaces through electrostatic interactions.

The adsorption capacity and photocatalytic activity of non-doped and Ce-doped Bi_2WO_6 and Bi_2WO_6-BiOCl samples were evaluated *via* the adsorption and photodegradation of salicylic acid in the dark and under visible light irradiation, respectively, and the results are shown in Fig. 7 and Table 1. The adsorption capacity of the synthesized samples for salicylic acid was directly proportional to the measured specific surface area. Specifically, the higher the specific surface area is, the greater the adsorption capacity is. With an increasing content of Ce dopants, the specific surface area and adsorption of salicylic acid gradually increase in the following order: 6.1 $m^2 \cdot g^{-1}$ and 7.2% (0 mol% Ce) < 6.7 $m^2 \cdot g^{-1}$ and 8.8% (0.5 mol%) < 7.3 $m^2 \cdot g^{-1}$ and 11.6% (1 mol%) < 9.4 $m^2 \cdot g^{-1}$ and 14.0% (2 mol%) < 11.6 $m^2 \cdot g^{-1}$ and 17.6% (4 mol%) < 14.2 $m^2 \cdot g^{-1}$ and 23.2% (6 mol%) < 15.8 $m^2 \cdot g^{-1}$ and 25.6% (8 mol%) < 18.3 $m^2 \cdot g^{-1}$ and 30.4% (10 mol%) for Bi_2WO_6 and 9.6 $m^2 \cdot g^{-1}$ and 11.6% (0 mol%) < 11.4 $m^2 \cdot g^{-1}$ and 14.0% (0.5 mol%) < 14.8 $m^2 \cdot g^{-1}$ and 21.6% (1 mol%) < 18.7 $m^2 \cdot g^{-1}$ and 27.2% (2 mol%) < 29.5 $m^2 \cdot g^{-1}$ and 34.0% (4 mol%) < 36.9 $m^2 \cdot g^{-1}$ and 35.6% (6 mol%) < 40.2 $m^2 \cdot g^{-1}$ and 39.2% (8 mol%) < 48.6 $m^2 \cdot g^{-1}$ and 43.6% (10 mol%) for Bi_2WO_6-BiOCl. In contrast, the photodegradation of salicylic acid over the synthesized samples did not follow this

Please cite this article in press as: Hojamberdiev, M. et al., Tuning the morphological structure, light absorption, and photocatalytic activity of Bi_2WO_6 and Bi_2WO_6-BiOCl through cerium doping. Arabian Journal of Chemistry (2018), https://doi.org/10.1016/j.arabjc.2018.07.014

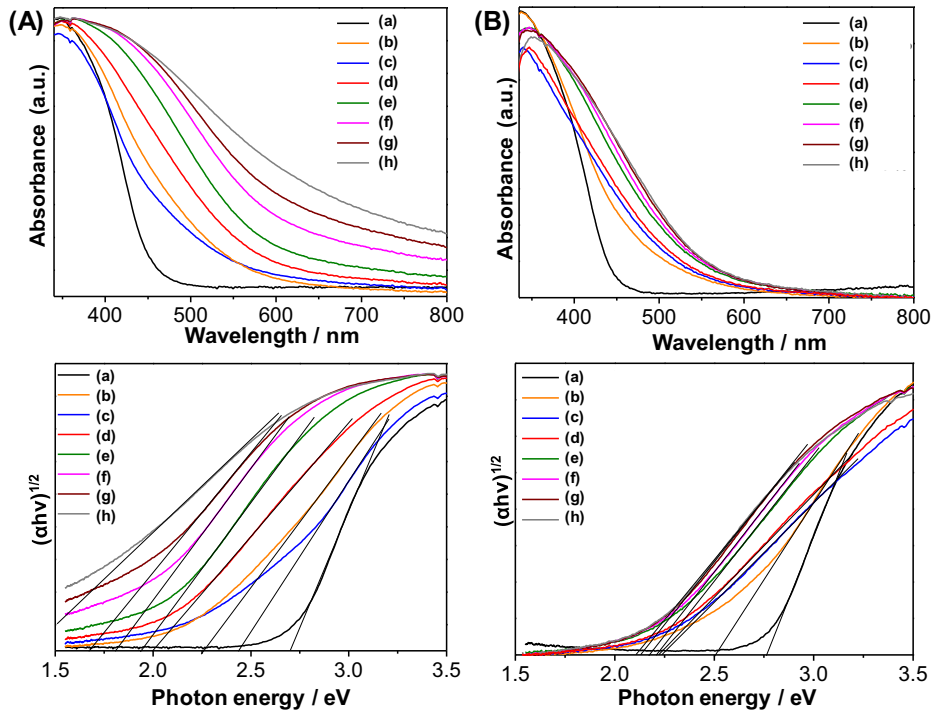

Fig. 5 UV–vis diffuse reflectance spectra (*top*) and Tauc plots (*bottom*) of Bi_2WO_6 (A) and Bi_2WO_6-BiOCl (B) powders doped with different contents of cerium: (a) 0 mol%, (b) 0.5 mol%, (c) 1 mol%, (d) 2 mol%, (e) 4 mol%, (f) 6 mol%, (g) 8 mol%, and (h) 10 mol%.

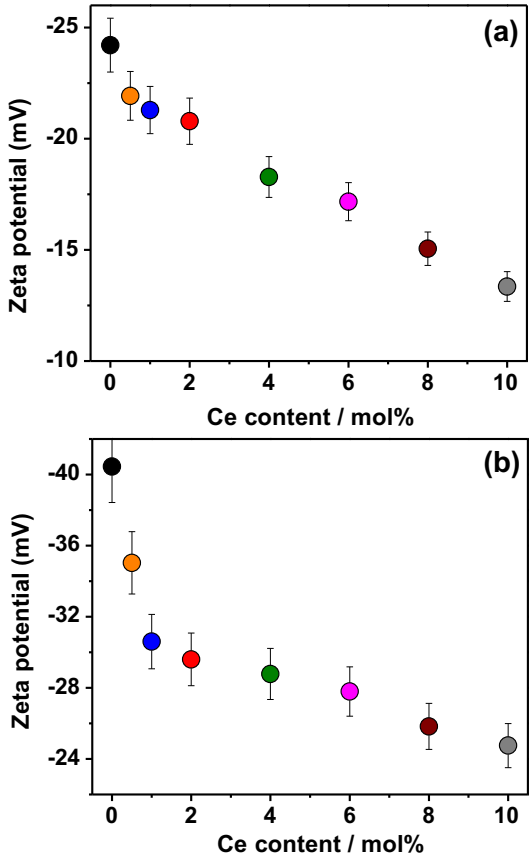

Fig. 6 Zeta potential of (a) Bi_2WO_6 and (b) Bi_2WO_6-BiOCl powders at neutral pH as a function of cerium dopant content.

trend. The results indicate that cerium doping has not only tuned the morphological structure but also increased the specific surface area, improving the adsorption capacity of Bi_2WO_6 and Bi_2WO_6-BiOCl for salicylic acid.

The adsorption affinities and preferential sites of salicylic acid molecules on non-doped and Ce-doped Bi_2WO_6, BiOCl, and Bi_2WO_6-BiOCl were computationally studied using molecular dynamics simulations (Hojamberdiev et al. (2017a,b)). The adsorption of salicylic acid molecules onto the surfaces is visually illustrated in Figs. 8 and 9. The adsorption energies of the most stable configuration of a salicylic acid molecule and a water molecule over mineral surfaces were exothermic due to the strong mineral–adsorbate interaction (Fig. 8). The simultaneous adsorption of the salicylic acid and water molecules on the Ce-doped Bi_2WO_6 mineral is stronger (more exothermic) than that on Bi_2WO_6 ($\Delta_{ads} = (E_{ads}(HSal + H_2O) - (E_{ads}(HSal) + E_{ads}(H_2O))_{Bi2WO6}$-$(E_{ads}(HSal + H_2O) - (E_{ads}(HSal) + E_{ads}(H_2O))_{Ce\text{-}doped\ Bi2WO6} = 10$ kcal·mol^{-1}). However, the Δ_{ads} value is less (0.25 kcal·mol^{-1}) for the Ce-doped BiOCl surface than the BiOCl surface. The obtained results can be explained via an approximation of the formation of different electronic structures of the adsorbed layer of water molecules that interact with the mineral surface through the H-bonds network and close contact. The adsorbed salicylic acid molecules can be stabilized by interaction with the layer of water molecules and direct interaction with the mineral surface. The salicylic acid molecules can interact with the surface atoms using the carboxyl ($O_{C=O}$, O_{COH}, H_{COOH}) and hydroxyl (O_{OH}, H_{OH}) groups.

Fig. 9 shows the most stable molecular configurations with H bonds over the Bi_2WO_6, Ce-doped Bi_2WO_6, BiOCl, and Ce-doped BiOCl surfaces:

Please cite this article in press as: Hojamberdiev, M. et al., Tuning the morphological structure, light absorption, and photocatalytic activity of Bi_2WO_6 and Bi_2WO_6-BiOCl through cerium doping. Arabian Journal of Chemistry (2018), https://doi.org/10.1016/j.arabjc.2018.07.014

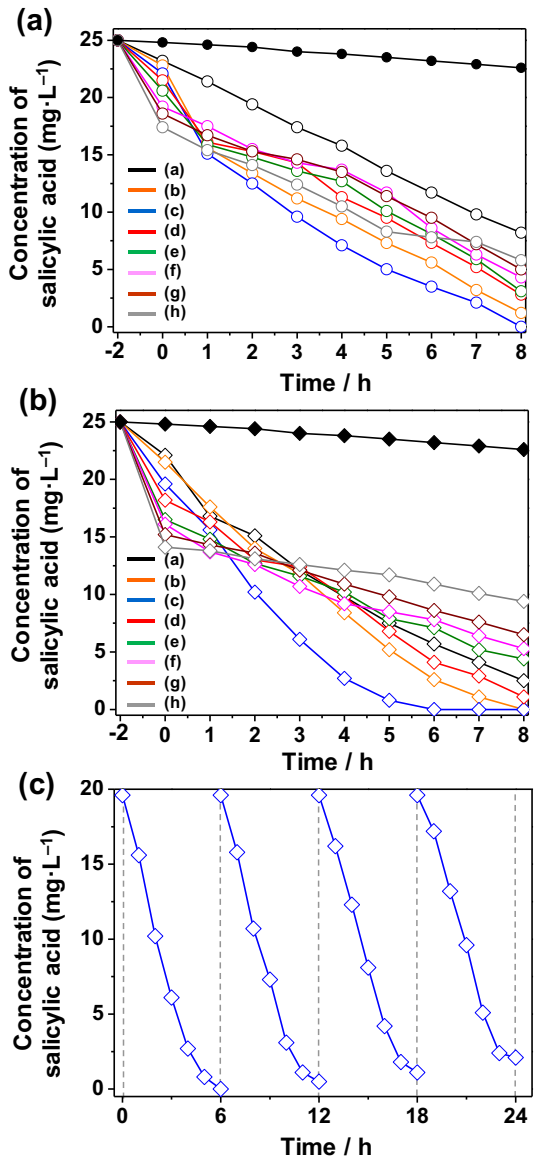

Fig. 7 Adsorption and photocatalytic activity for the removal of salicylic acid of (a) Bi_2WO_6 and (b) Bi_2WO_6-BiOCl powders doped with different contents of cerium ranging from 0 mol% to 10 mol%. (c) Photocatalytic activity for the degradation of salicylic acid over the Bi_2WO_6-BiOCl powders doped with 1 mol % Ce for four cycles.

(i) *Salicylic acid adsorption model*. Over the Bi_2WO_6 and Ce-doped Bi_2WO_6 surfaces, salicylic acid molecules have an intramolecular H bond ($O_{COH}...H_{COOH}$ – 2.354 Å) and prefer to connect to the surface oxygen atoms directly ($H_{COOH}...O{-}Bi$ – 2.736 and 2.739 Å). The BiOCl surface contacts the salicylic acid molecules via $H_{COOH}...Cl$ – 2.932 Å, whereas the Ce-doped BiOCl surface has no H bonds except a typical intramolecular H bond ($O_{COH}...H_{COOH}$ – 2.322 Å).

(ii) *Water adsorption model*. The layered structure of the adsorbed water molecules differs for the Bi_2WO_6 and Ce-doped Bi_2WO_6 surfaces. Over the Bi_2WO_6 surface, the water molecules form a monolayer with intermolecular H bonds ($O_{H2O}...H_{H2O}$ – 2.443–2.669 Å) and interact with the surface ($H_{H2O}...O{-}W$ – 2.774–2.902 Å, $H_{H2O}...O{-}Bi$ – 2.851–2.983 Å). However, over the Ce-doped Bi_2WO_6 surface, the water molecules form separated agglomerates that are in contact with the surface ($H_{H2O}...O{-}W$ – 2.989–2.905 Å), whereas the H bond provides the possibility for the salicylic acid molecules to enter the surface directly. However, over the Bi_2WO_6 and Ce-doped Bi_2WO_6 surfaces, the salicylic acid molecules have no direct interaction with the surface and connect to the layer of water molecules by the intermolecular H bonding. The results from the zeta-potential analysis of the Bi_2WO_6 and Ce-doped Bi_2WO_6 particles confirm the formation of a layer of water molecules on the mineral surface. Over the BiOCl and Ce-doped BiOCl surfaces, the water molecules are chained by H bonds ($O_{H2O}...H_{H2O}$ – 2.443–2.669 Å) without a strong interaction with the surface (close contacts H...Cl – 3.1 Å). The layer of water molecules over the Ce-doped BiOCl surface exhibits much closer contact H...Cl and some periodical order depending on the presence of Ce atoms.

(iii) *Salicylic acid and water adsorption model*. The salicylic acid molecules prefer to bind to the surface oxygen atoms indirectly through the water molecules that are already in contact with the Bi_2WO_6 ($H_{H2O}...O{-}W$ – 2.741–2.805 Å) and Ce-doped Bi_2WO_6 ($H_{H2O}...O{-}Bi$ – 2.763, $H_{H2O}...O{-}W$ – 2.835–2.954, and $H_{H2O}...O{-}Ce$ – 2.854 Å). The BiOCl surface directly binds with the salicylic acid molecules via H bonding ($H_{COOH}...Cl$ – 2.932 Å), the water molecules involved in the H-bond network with the salicylic acid molecules ($O_{OH}...H_2O$, $O_{C=O}...H_2O$, $O_{COOH}...H_2O$) and other water molecules. The Ce-doped BiOCl surface has demonstrated no direct bonding to the salicylic acid molecules, which involve the layer of water molecules located over the surface using close contacts $Cl...H_2O$ – 3.133–3.148 Å. The field density shows separated spaces breaking near the randomly distributed Ce atoms (Fig. 8).

The results indicate that the Ce-doped Bi_2WO_6 surface exhibits a better interaction with the salicylic acid and water molecules, resulting in higher photocatalytic activity, as predicted by the molecular dynamics calculations. Interestingly, the Ce-doped BiOCl surface possesses no pronounced impact on the adsorption of salicylic acid molecules, but the positive effect of the combination of the high specific surface area and electronic interaction between the salicylic acid and layer of water molecules is observed for the Ce-doped Bi_2WO_6-BiOCl sample.

The photodegradation efficiency of salicylic acid over the synthesized samples was estimated based on the change in the intensity of absorption peaks of salicylic acid at 296 nm and the results of the total organic carbon (TOC) analysis. As shown in Fig. 7a and b, the direct photolysis of salicylic acid performed for comparison under identical experimental conditions in the absence of photocatalysis was negligible, indicating that salicylic acid is stable under visible light irradiation. In both cases, the photodegradation efficiency of salicylic acid over the synthesized samples at 5 h gradually reaches the maximum (91.6% for Bi_2WO_6 and 96.8% for Bi_2WO_6-BiOCl) at 1 mol% Ce.

Table 1 Adsorption and photodegradation of salicylic acid over the non-doped and Ce-doped Bi_2WO_6 and Bi_2WO_6-BiOCl.

Sample	S_{BET}	Salicylic acid adsorption in the dark		Salicylic acid photodegradation under visible light irradiation	
Ce-doped Bi_2WO_6	$m^2 \cdot g^{-1}$	μmol	%	% at 5 h	k, min^{-1}
0 mol%	6.1	23.2	7.2	60.8	−0.105
0.5 mol%	6.7	22.8	8.8	87.2	−0.233
1 mol%	7.3	22.1	11.6	91.6	−0.297
2 mol%	9.4	21.5	14.0	79.2	−0.159
4 mol%	11.6	20.6	17.6	76.4	−0.137
6 mol%	14.2	19.2	23.2	74.8	−0.095
8 mol%	15.8	18.6	25.6	71.2	−0.090
10 mol%	18.3	17.4	30.4	70.4	−0.147
Ce-doped Bi_2WO_6-BiOCl	$m^2 \cdot g^{-1}$	μmol	%	% at 5 h	k, min^{-1}
0 mol%	9.6	22.1	11.6	70.0	−0.224
0.5 mol%	11.4	21.5	14.0	79.2	−0.250
1 mol%	14.8	19.6	21.6	96.8	−0.360
2 mol%	18.7	18.2	27.2	72.8	−0.169
4 mol%	29.5	16.5	34.0	68.4	−0.136
6 mol%	36.9	16.1	35.6	66.0	−0.128
8 mol%	40.2	15.2	39.2	60.8	−0.092
10 mol%	48.6	14.1	43.6	53.2	−0.040

A further increment in the Ce content up to 10 mol% gradually decreased the photodegradation efficiency of salicylic acid over the Bi_2WO_6 and Bi_2WO_6-BiOCl samples. Excess Ce species possibly covered the active sites or acted as a recombination center, reducing the separation efficiency of the charge carriers. Therefore, 1 mol% was found to be the optimum concentration of Ce doping in Bi_2WO_6 and Bi_2WO_6-BiOCl, promoting the effective separation and transfer of photogenerated charge carriers, resulting in high photocatalytic performance. Compared to Bi_2WO_6, the Bi_2WO_6-BiOCl samples exhibited higher photocatalytic activity owing to the formation of a *p–n* heterojunction in the composite. The experimentally obtained data were fitted in the pseudo first-order kinetic equation $\ln(C/C_0) = -kt$, and the apparent rate constants of the photodegradation of salicylic acid are given in Table 1. Among the samples, the 1 mol% Ce-doped Bi_2WO_6-BiOCl sample showed the highest apparent rate constant ($k = -0.360\ min^{-1}$), which is more than three times higher than that of non-doped Bi_2WO_6 ($k = -0.105\ min^{-1}$), due to the synergistic effect of cerium doping and the formed *p–n* heterojunction. For future practical applications, it is important to investigate the reusability and stability of the synthesized materials during a photocatalytic reaction. In this context, the 1 mol% Ce-doped Bi_2WO_6-BiOCl sample was subjected to four successive photocatalytic experiments by adding a fresh aqueous solution containing salicylic acid in each run under visible light irradiation. As shown in Fig. 7c, the photodegradation efficiency of salicylic acid over the sample slightly decreased due to the loss of photocatalyst particles during the separation after each cycle, suggesting that the synthesized composite has good stability and can be consecutively used in water purification processes.

Based on the above results and previous reports, a possible mechanism for the enhanced photocatalytic activity of the Bi_2WO_6-BiOCl composite for the degradation of salicylic acid is schematically illustrated in Fig. 10. When *p*-type BiOCl and *n*-type Bi_2WO_6 are in contact, a *p–n* heterojunction forms, resulting in the formation of an internal electric field at the interface of the *p–n* heterojunction after equilibrium. The formed heterojunction in turn accelerates the separation of photogenerated electron-hole pairs (Chen et al., 2018). According to the calculated data reported previously (Yang et al., 2013), in the Bi_2WO_6-BiOCl heterojunction, the electrons in the conduction band of BiOCl transfer to the conduction band of Bi_2WO_6 because the conduction band of the latter is more positively positioned than that of the former. Simultaneously, additional electrons are excited to the conduction band of Bi_2WO_6 under visible light irradiation. The transferred and excited electrons can reduce O_2 to $\cdot O_2^-$ and transform into $\cdot OH$. Meanwhile, the holes in the valence band of Bi_2WO_6 transfer to the valence band of BiOCl because the valence band of BiOCl is more negatively located than that of Bi_2WO_6 and oxidize H_2O and OH^- to $\cdot OH$. Along with the holes, the generated $\cdot OH$ by both electrons and holes will be involved in the degradation of salicylic acid under visible light (Hojamberdiev et al., 2017a,b; Li et al. 2017b; Zhu et al., 2015).

As the holes and electrons are separated in the valence band of BiOCl and the conduction band of Bi_2WO_6, respectively, the formed Bi_2WO_6-BiOCl heterojunction therefore possesses a lower recombination rate of photogenerated electrons and holes at the interface, contributing to the enhanced photocatalytic activity:

$$\text{Ce-doped } Bi_2WO_6\text{-BiOCl} + h\nu \rightarrow \text{Ce-doped } Bi_2WO_6\text{-BiOCl}(e^- + h^+) \quad (1)$$

$$\text{Ce-doped } Bi_2WO_6\text{-BiOCl}(e_{CB}^-) + O_{2(ads.)} \rightarrow \text{Ce-doped } Bi_2WO_6\text{-BiOCl} + \cdot O_2^-(\text{ads.})(\text{electron trapping by } O_2 \text{ adsorption}) \quad (2)$$

$$2 \cdot O^{2-} + 2e^- + 2H^+ \rightarrow 2H_2O_2 \quad (3)$$

$$H_2O_2 + e^- + H^+ \rightarrow 2 \cdot OH \quad (4)$$

$$H_2O + h^+ \rightarrow \cdot OH + H^+ \quad (5)$$

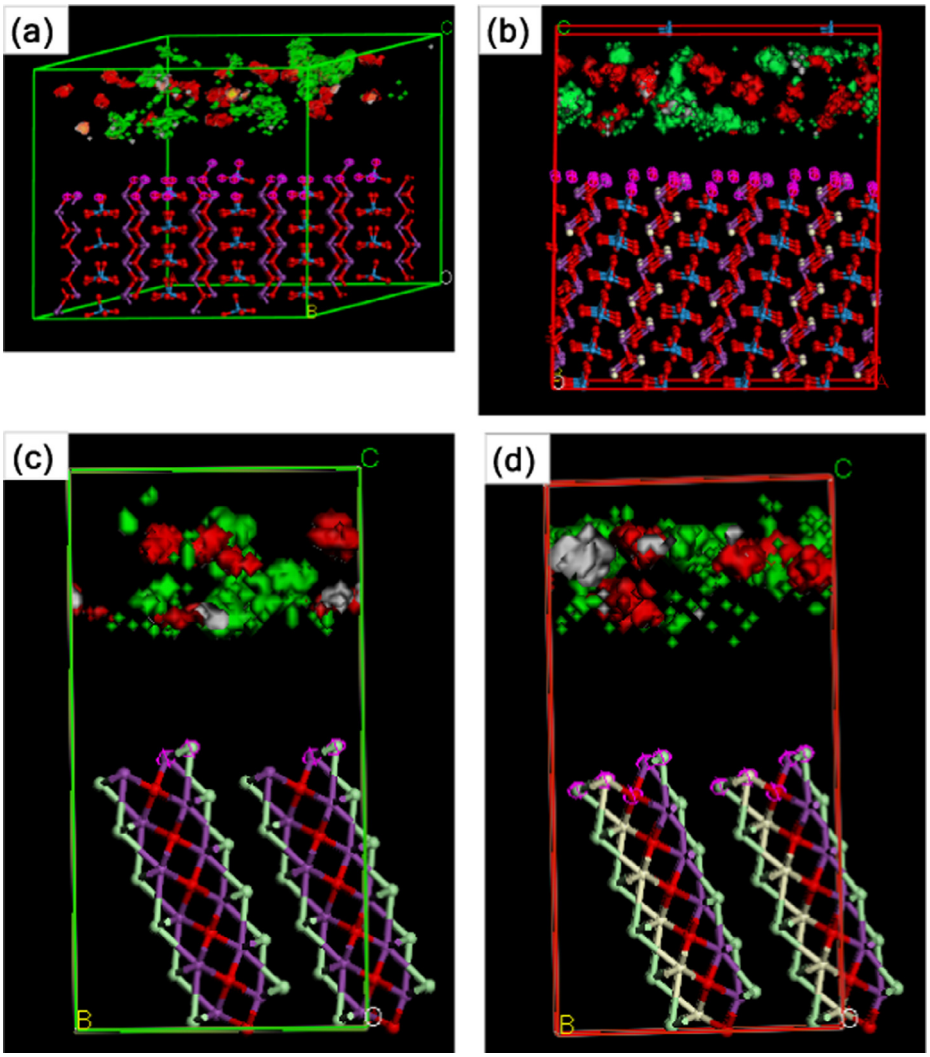

Fig. 8 Visualization of adsorption of the salicylic acid and water molecules onto (1 1 1) cleavage surfaces of (a) Bi_2WO_6, (b) Ce-doped Bi_2WO_6, (c) BiOCl, and (d) Ce-doped BiOCl: bismuth, violet; tungsten, blue; oxygen, red; chlorine, light-green; and cerium, beige. Density isosurface: salicylic acid, red; water, green.

$$(C_7H_6O_3)_{ads} + {}^{\cdot}OH \rightarrow (C_7H_6O_3)_{ads}{}^{+} \rightarrow (\text{Intermediate})_{ads} \rightarrow CO_2 + H_2O + \text{by-products} \quad (6)$$

$$(C_7H_6O_3)_{ads} + h^{+} \rightarrow (C_7H_6O_3)_{ads}{}^{+} \rightarrow (\text{Intermediate})_{ads} \rightarrow CO_2 + H_2O + \text{by-products} \quad (7)$$

Although the formation of the intermediates is complex and not particularly investigated in the present work, it is thought that the photodegradation of salicylic acid over the Bi_2WO_6 and Bi_2WO_6-BiOCl samples follows the most likely reaction pathway, resulting in the formation of 1,2-dihydroxybenzene, 2,3-dihydroxybenzoic acid, hydroquinone, benzoquinone, muconic acid, maleic acid, oxalic acid, malic acid, malonic acid, and acetic acid as intermediates, which explains the opening of the aromatic ring (Mukherjee et al., 2016). Previously, a high degree of mineralization of salicylic acid over TiO_2/SiO_2 fibers was achieved through the homogeneous photochemical oxidation by adding an adequate amount of H_2O_2 due to the formation of ·OH radicals (Adán et al., 2006). Arfanis et al. (2017) reported that TiO_2 nanotubular films showed a negligible variation in their photocatalytic activity towards the photodegradation of salicylic acid in a wide pH range of aqueous solutions, making them suitable for applications under different conditions. Lang et al. (1996) suggested that salicylic acid molecules can also act as sensitizers for photochemical oxidation by absorbing photons at higher wavelengths, which contributes to the photocatalytic activity.

As the Bi_2WO_6 amount in the composite gradually decreases with increasing Ce content, a decrease in the photocatalytic activity is observed, demonstrating the pivotal role of the formed heterojunction. The improvement in the photocatalytic activity of the samples doped with an appropriate amount of cerium stems from (i) the presence of a Ce^{3+}/Ce^{4+} redox couple that can act as an electron scavenger and superoxide radicals ($^{\cdot}O_2^{-}$) producers, (ii) the formation of oxygen vacancies with the relatively high mobility of bulk oxygen species, and (iii) the different optical properties that result from the various electronic structures of Ce^{3+} with $4f^15d^0$ and Ce^{4+} with $4f^05d^0$. During the reaction, the photogener-

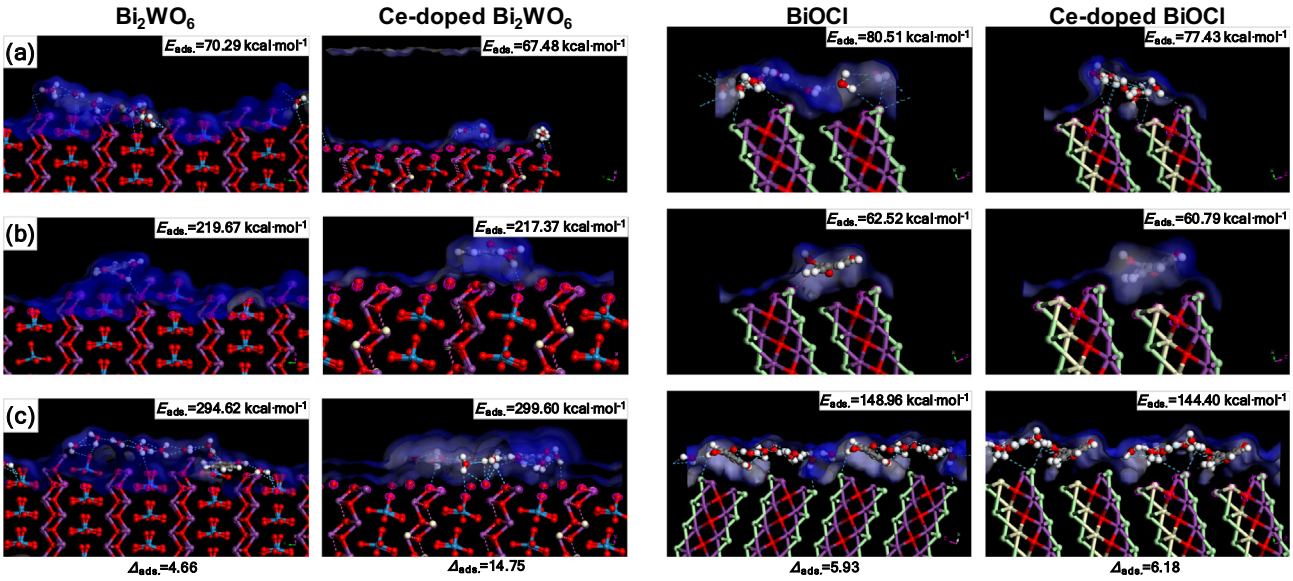

Fig. 9 Structure model of adsorption of (a) water molecules, (b) salicylic acid molecules, and (c) water and salicylic acid molecules: bismuth, violet; tungsten blue; oxygen, red; chlorine, light-green; and cerium, beige. Isosurface: Connolly surface, blue.

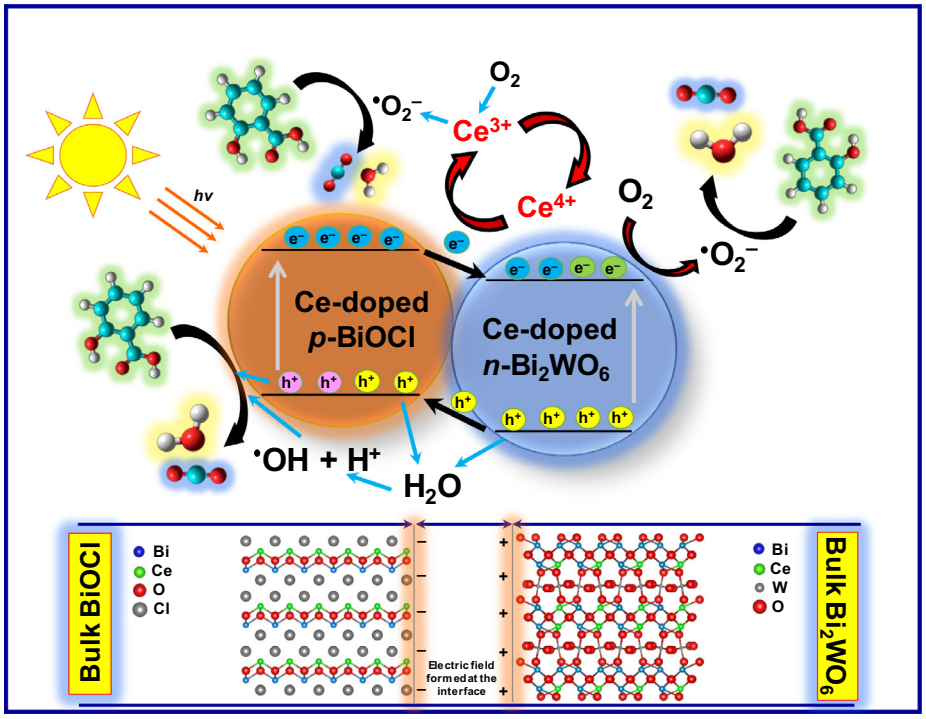

Fig. 10 Schematic representation of the photodegradation mechanism of salicylic acid over the Bi_2WO_6-BiOCl powders doped with 1 mol% Ce under visible light irradiation.

ated electrons are trapped by Ce^{4+}, and Ce^{4+} is reduced to Ce^{3+}, which can be oxidized back to Ce^{4+} by the adsorbed oxygen in the system. The adsorbed oxygen reacts with Ce^{3+} and e^- to produce $\cdot O_2^-$. In addition to the efficient separation of electrons and holes, the Ce^{3+}/Ce^{4+} redox couple also promotes the generation of $\cdot O_2^-$ that can also contribute to the improvement of photocatalytic activity along with the ·OH and holes (Hojamberdiev et al. (2017a,b); Huang et al., 2014; Hojamberdiev et al., 2014):

$$Ce^{4+} + e^- \rightarrow Ce^{3+}(\text{electron trapping}) \quad (8)$$

$$Ce^{3+} + O_2 \rightarrow Ce^{4+} + \cdot O_2^-(\text{electrontransfer}) \quad (9)$$

$$(C_7H_6O_3)_{ads} + \cdot O_2^- \rightarrow (\text{intermediate})_{ads} \rightarrow CO_2 + H_2O \quad (10)$$

Please cite this article in press as: Hojamberdiev, M. et al., Tuning the morphological structure, light absorption, and photocatalytic activity of Bi_2WO_6 and Bi_2WO_6-BiOCl through cerium doping. Arabian Journal of Chemistry (2018), https://doi.org/10.1016/j.arabjc.2018.07.014

The obtained results showed that the synthesized materials can be used for the purification of water contaminated with various pharmaceuticals and personal care products.

4. Conclusions

In summary, we have successfully synthesized non-doped and Ce-doped Bi_2WO_6 and Bi_2WO_6-BiOCl powders by a hydrothermal method. The Bi_2WO_6-BiOCl composite was formed when ethylene glycol was replaced by dilute HCl as a solvent in the hydrothermal system. The formation of flower-like morphologies was governed by a complexing agent (ethylene glycol) forming a chain-like structure on the crystallite surface and the selective adsorption of excessive Cl^- ions on the specific surface of crystallite, leading to a morphological variation. Cerium doping could extend the absorption edges of Bi_2WO_6 and Bi_2WO_6-BiOCl up to 460 and >700 nm, respectively. According to the molecular dynamics calculation results, Ce doping enhances the interaction of the Bi_2WO_6 surface with the salicylic acid molecules in Ce-doped Bi_2WO_6-BiOCl due to the improved interaction between the Bi_2WO_6 surface and the layer of water molecules through which the salicylic acid molecules are connected by hydrogen bonding. Among the samples, the 1 mol% Ce-doped Bi_2WO_6-BiOCl sample showed the highest apparent rate constant ($k = -0.360\ min^{-1}$), which is more than three times higher than that of non-doped Bi_2WO_6 ($k = -0.105\ min^{-1}$), due to the synergistic effect of cerium doping and the formed *p–n* heterojunction. More importantly, the synthesized composite possesses good photostability and can be reused during water treatment.

5. Declarations of interest.

None.

Acknowledgment

MH would like to thank the TWAS-UNESCO Associateship and Japan Society for the Promotion of Science (JSPS) for the postdoctoral fellowship under which the present study was carried out.

References

Adán, C., Coronado, J.M., Bellod, R., Soria, J., Yamaoka, H., 2006. Photochemical and photocatalytic degradation of salicylic acid with hydrogen peroxide over TiO_2/SiO_2 fibres. Appl. Catal. A 303, 199–206.

An, J., Tang, B., Zheng, X., Zhou, J., Dong, F., Xu, S., Wang, Y., Zhao, B., Xu, W., 2008. Sculpturing effect of chloride ions in shape transformation from triangular to discal silver nanoplates. J. Phys. Chem. C 112, 15176–15182.

Arfanis, M.K., Adamou, P., Moustakas, N.G., Triantis, T.M., Kontos, A.G., Falaras, P., 2017. Photocatalytic degradation of salicylic acid and caffeine emerging contaminants using titania nanotubes. Chem. Eng. J. 310, 525–536.

Chen, Y., Zhu, G., Hojamberdiev, M., Gao, J., Zhu, R., Wang, C., Wei, X., Liu, P., 2018. Three-dimensional Ag2O/Bi5O7I p–n heterojunction photocatalyst harnessing UV–Vis–NIR broad spectrum for photodegradation of organic pollutants. J. Hazard. Mater. 344, 42–54.

Cui, Z., Yang, H., Wang, B., Li, R., Wang, X., 2016. Effect of experimental parameters on the hydrothermal synthesis of Bi_2WO_6 nanostructures. Nanoscale Res. Lett. 11, 190.

Evgenidou, E.N., Konstantinou, I.K., Lambropoulou, D.A., 2015. Occurrence and removal of transformation products of PPCPs and illicit drugs in wastewaters: a review. Sci. Total Environ. 505, 905–926.

Francisco, M.S.P., Mastelaro, V.R., Nascente, P.A.P., Florentino, A. O., 2001. Activity and characterization by XPS, HR-TEM, Raman spectroscopy, and BET surface area of CuO/CeO_2-TiO_2 catalysts. J. Phys. Chem. B 105, 10515–10522.

Garza-Campos, B., Brillas, E., Hernández-Ramírez, A., El-Ghenymy, A., Guzmán-Mar, J.L., Ruiz-Ruiz, E.J., 2016. Salicylic acid degradation by advanced oxidation processes. Coupling of solar photoelectro-Fenton and solar heterogeneous photocatalysis. J. Hazard. Mater. 319, 34–42.

Hojamberdiev, M., Kadirova, Z.C., Gonçalves, R.V., Yubuta, K., Matsushita, N., Teshima, K., Hasegawa, M., Okada, K., 2018. Reduced graphene oxide-modified Bi_2WO_6/BiOI composite for the effective photocatalytic removal of organic pollutants and molecular modeling of adsorption. J. Mol. Liquids. https://doi.org/10.1016/j.molliq.2018.07.110. in press.

Hojamberdiev, M., Kadirova, Z.C., Makinose, Y., Zhu, G., Emin, S., Matsushita, N., Hasegawa, M., Okada, K., 2017a. Involving $CeVO_4$ in improving the photocatalytic activity of a Bi_2WO_6/allophane composite for the degradation of gaseous acetaldehyde under visible light. Colloids Surf. A 529, 600–612.

Hojamberdiev, M., Kadirova, Z.C., Makinose, Y., Zhu, G., Matsushita, N., Rodríguez, J., Aldabe Bilmes, S., Hasegawa, M., Okada, K., 2017b. Influence of BiOI content on the photocatalytic activity of Bi_2WO_6/BiOI/allophane composites and molecular modeling studies of acetaldehyde adsorption. J. Taiwan Inst. Chem. Eng. 81, 258–264.

Hojamberdiev, M., Katsumata, K.-I., Morita, K., Aldabe Bilmes, S., Matsushita, N., Okada, K., 2013. One-step hydrothermal synthesis and photocatalytic performance of $ZnWO_4/Bi_2WO_6$ composite photocatalyst for efficient degradation of acetaldehyde under UV light irradiation. Appl. Catal. A 457, 12–20.

Hojamberdiev, M., Katsumata, K.-I., Matsushita, N., Okada, K., 2014. Preparation of Bi_2WO_6– and BiOI–allophane composites for efficient photodegradation of gaseous acetaldehyde under visible light. Appl. Clay Sci. 101, 38–43.

Huang, H., Liu, K., Chen, K., Zhang, Y., Zhang, Y., Wang, S., 2014. Ce and F comodification on the crystal structure and enhanced photocatalytic activity of Bi_2WO_6 photocatalyst under visible light irradiation. J. Phys. Chem. C 118, 14379–14387.

Ju, P., Wang, P., Li, B., Fan, H., Ai, S., Zhang, D., Wang, Y., 2014. A novel calcined $Bi_2WO_6/BiVO_4$ heterojunction photocatalyst with highly enhanced photocatalytic activity. Chem. Eng. J. 236, 430–437.

Kosma, C.I., Lambropoulou, D.A., Albanis, T.A., 2014. Investigation of PPCPs in wastewater treatment in Greece: occurrence removal and environmental risk assessment. Sci. Total Environ. 466–467, 421–438.

Lang, K., Brodilová, J., Luňák, S., 1996. Photochemical hydroxylation of salicylic acid with hydrogen peroxide; mechanistic study of substrate sensitized reaction. Collect. Czech. Chem. Commun. 61, 1729–1737.

Li, H., Hao, H., Jin, S., Guo, W., Hu, X., Hou, H., Zhang, G., Yan, S., Gao, W., Liu, G., 2017a. Synthesis of Yb^{3+}/Ho^{3+} co-doped Bi_2WO_6 upconversion photocatalyst with highly improved visible light photocatalytic activity. Catal. Commun. 97, 60–64.

Li, S., Bian, X., Gao, J., Zhu, G., Hojamberdiev, M., Wang, C., Wei, X., 2017b. Effect of oxygen vacancy and surface plasmon resonance: a photocatalytic activity study on $Ag/Bi_4Ti_3O_{12}$ nanocomposites. J. Mater. Sci.: Mater. Electron. 28, 17896–17907.

Li, Y., Liu, Y., Wang, J., Uchaker, E., Zhang, Q., Sun, S., Huang, Y., Li, J., Cao, G., 2013. Titanium alkoxide induced BiOBr–Bi_2WO_6

mesoporous nanosheet composites with much enhanced photocatalytic activity. J. Mater. Chem. A 1, 7949–7956.

Ma, R., Wang, X., Huang, J., Song, J., Zhang, J., Wang, X., 2017. Photocatalytic degradation of salicylic acid with magnetic activated carbon-supported F-N codoped TiO_2 under visible light. Vacuum 141, 157–165.

Mukherjee, D., Ray, A.K., Barghi, S., 2016. Mechanism of acetyl salicylic acid (Aspirin) degradation under solar light in presence of a TiO_2-polymeric film photocatalyst. Processes 4, 1–9.

Peng, Y., Chen, Q.-G., Wang, D., Zhou, H.-Y., Xu, A.-W., 2015. Synthesis of one-dimensional WO_3–Bi_2WO_6 heterojunctions with enhanced photocatalytic activity. CrystEngComm 17, 569–576.

SCCNFP/0522/01, final. Opinion of the scientific committee on cosmetic products and non-food products intended for consumers concerning salicylic acid, 4 June 2002. http://ec.europa.eu/health/ph_risk/committees/sccp/documents/out170_en.pdf.

Sirés, I., Brillas, E., 2012. Remediation of water pollution caused by pharmaceutical residues based on electrochemical separation and degradation technologies: a review. Environ. Int. 40, 212–229.

Stamatis, N.K., Konstantinou, I.K., 2013. Occurrence and removal of emerging pharmaceutical, personal care compounds and caffeine tracer in municipal sewage treatment plant in Western Greece. J. Environ. Sci. Health B 48, 800–813.

Tian, N., Zhang, Y., Huang, H., He, Y., Guo, Y., 2014. Influences of Gd substitution on the crystal structure and visible light-driven photocatalytic performance of Bi_2WO_6. J. Phys. Chem. C 118, 15640–15648.

Tian, Y., Zhang, L., Zhang, J., 2012. A superior visible light-driven photocatalyst: europium-doped bismuth tungstate hierarchical microspheres. J. Alloy. Compd. 537, 24–28.

Wang, C., Zhu, Q., Gu, C., Luo, X., Yu, C., Wu, M., 2016a. Photocatalytic degradation of two different types of dyes by synthesized La/Bi_2WO_6. RSC Adv. 6, 85852–85859.

Wang, F., Li, W., Gu, S., Li, H., Wu, X., Liu, X., 2016b. Samarium and nitrogen co-doped Bi_2WO_6 photocatalysts: synergistic effect of Sm^{3+}/Sm^{2+} redox centers and N-doped level for enhancing visible-light photocatalytic activity. Chem. Eur. J. 22, 12859–12867.

Wang, M., Qiao, Z., Fang, M., Huang, Z., Liu, Y., Wu, X., Tang, C., Tang, H., Zhu, H., 2015. Synthesis of Er-doped Bi_2WO_6 and enhancement in photocatalytic activity induced by visible light. RSC Adv. 5, 94887–94894.

Wang, X., Wan, X., Chang, L., 2014. Solvothermal synthesis of Bi_2WO_6 hollow microspheres via Ostwald ripening with their enhanced photocatalytic activity. Catal. Lett. 144, 1268–1277.

Xiang, Y., Ju, P., Wang, Y., Sun, Y., Zhang, D., Yu, J., 2016. Chemical etching preparation of the Bi_2WO_6/BiOI *p–n* heterojunction with enhanced photocatalytic antifouling activity under visible light irradiation. Chem. Eng. J. 288, 264–275.

Xu, K., Fu, X., Peng, Z., 2018. Facile synthesis and photocatalytic activity of La-doped BiOCl hierarchical, flower-like nano-/microstructures. Mater. Res. Bull. 98, 103–110.

Xu, X., Shen, X., Zhu, G., Jing, L., Liu, X., Chen, K., 2012. Magnetically recoverable Bi_2WO_6–Fe_3O_4 composite photocatalysts: Fabrication and photocatalytic activity. Chem. Eng. J. 200–202, 521–531.

Yang, W., Ma, B., Wang, W., Wen, Y., Zeng, D., Shan, B., 2013. Enhanced photosensitized activity of a BiOCl–Bi_2WO_6 heterojunction by effective interfacial charge transfer. PCCP 15, 19387–19394.

Ye, L., Su, Y., Jin, X., Xie, H., Zhang, C., 2014. Recent advances in BiO*X* (X = Cl, Br and I) photocatalysts: synthesis, modification, facet effects and mechanisms. Environ. Sci. Nano 1, 90–112.

Zhang, N., Ciriminna, R., Pagliaro, M., Xu, Y.-J., 2014. Nanochemistry-derived Bi_2WO_6 nanostructures: towards production of sustainable chemicals and fuels induced by visible light. Chem. Soc. Rev. 43, 5276–5287.

Zhu, G., Liang, J., Hojamberdiev, M., Aldabe Bilmes, S., Wei, X., Liu, P., Zhou, J., 2014. Ethylenediamine (EDA)-assisted hydrothermal synthesis of nitrogen-doped Bi_2WO_6 powders. Mater. Lett. 122, 216–219.

Zhu, G., Liu, Y., Hojamberdiev, M., Han, J., Rodríguez, J., Aldabe Bilmes, S., Liu, P., 2015. Thermodecomposition synthesis of porous β-Bi_2O_3/$Bi_2O_2CO_3$ heterostructured photocatalysts with improved visible light photocatalytic activity. New J. Chem. 39, 9557–9568.

Please cite this article in press as: Hojamberdiev, M. et al., Tuning the morphological structure, light absorption, and photocatalytic activity of Bi_2WO_6 and Bi_2WO_6-BiOCl through cerium doping. Arabian Journal of Chemistry (2018), https://doi.org/10.1016/j.arabjc.2018.07.014